Nano Energy 45 (2018) 52–60

Contents lists available at ScienceDirect

Nano Energy

journal homepage: www.elsevier.com/locate/nanoen

Full paper

# Origin of phase inhomogeneity in lithium iron phosphate during carbon coating

Yulong Liu[a], Jiajun Wang[a], Jian Liu[a], Mohammad Norouzi Banis[a], Biwei Xiao[a], Andrew Lushington[a], Wei Xiao[a,b], Ruying Li[a], Tsun-Kong Sham[b], Guoxian Liang[c,*], Xueliang Sun[a,*]

[a] Department of Mechanical and Materials Engineering, Western University, London, Ontario, Canada N6A 5B9
[b] Department of Chemistry, Western University, London, Ontario, Canada N6A 5B7
[c] Johnson Matthey Battery Materials Ltd., 280 Ave. Liberté, Candiac, Quebec, Canada J5R 6X1

ARTICLE INFO

*Keywords:*
$LiFePO_4$
Carbon coating
Secondary phase
Phase change
Lithium ion battery

ABSTRACT

Phase purity plays a vital role in achieving high capacity and long cycle life for lithium iron phosphate. Given that $LiFePO_4$ has lower electronic and ionic conductivity, carbon coating on fine particle surface is often used in order to improve the electrochemical performance of $LiFePO_4$. Unfortunately, the carbon coating process is an inherently reducing process that is difficult to control and often results in the over-reduction of $LiFePO_4$, turning it into iron phosphide. Our research here demonstrates the formation of a non-conductive $Fe_2P_2O_7$ phase during the carbon coating process on $LiFePO_4$. This phase formation is found to be dependent on particle size, temperature, and annealing atmosphere. Furthermore, these changes are found to directly associate with the change of the reducing potential. The finding in this work aims to guide and control the phase purity of carbon coated $LiFePO_4$ by identifying important parameters that need to be taken under consideration during the carbon coating process in an effort to realize excellent electrochemical performance.

## 1. Introduction

Carbon surface coating has been widely applied to lithium iron phosphate (LFP) for lithium ion batteries in order to improve electronic conductivity as well as provide favourable surface chemistry [1]. LFP, possessing an intrinsically lower electronic conductivity of $10^{-9}$ S cm$^{-1}$, has been effectively improved by carbon coating [2,3]. Since pioneering work conducted by Ravet et al. demonstrates excellent electrochemical performance after carbon coating on the LFP, [4,5] research in this field has attracted great attentions. Most reports are focused on the understanding the influence of carbon coating on bulk LFP rather than surface effects [5–8]. However, changes to stoichiometry and/or the formation of secondary phases on the surface/interface of LFP have been unclear due to the complex nature of the carbon coating procedure [9–12]. This process comprises of several reactions occurring simultaneously and is reliant on many factors such as volatility of lithium, [13,14] deposition/diffusion of carbon, [15,16] and redox of iron and/or phosphors [17]. Given the electrochemical importance of secondary phases, researchers have attempted to synthesize the LFP with alternative phase composition. Further, the influences of secondary phase on the electrochemical performance have been reported by many groups [16,17]. Previously, a $Fe_2P_2O_7$ secondary phase was detected on the surface of hydrothermal synthesized LFP. The origin of such impurity phase formation was that more $Fe_{Li}$ anitisite was formed at lower temperature than high temperature solid state reactions [18-20]. However, there is a lack of in-depth understanding on the complex relationship between phase distribution and particle size [12,15,21]. Furthermore, the precise control over the formation of secondary/impurity phases still remains elusive and difficult. As a result, a holistic understanding of surface phase homogeneity on LFP will greatly improve product uniformity for mass-production [22,23].

Recently, our work demonstrated the formation of a secondary surface impurity phase of $Fe_2P_2O_7$ when carbon coating on LFP. This process was hypothesized to occur due to loss of lithium oxide at high temperature [24]. With advanced in-depth characterization techniques, surface chemistry change was clearly visualized and recorded on the flat surface of ingot samples. The phase distribution on the surface of LFP was found to become inhomogeneous following the coating process as a result of C/LFP interface reactions. This $Fe_2P_2O_7$ phase is expected to be electrochemically inert, with no contribution to the capacity of LFP. The emerging question of importance that arises out of this study is what surface properties allow for the facile formation of secondary

* Corresponding authors.
*E-mail addresses:* Guoxian.Liang@matthey.com (G. Liang), xsun@eng.uwo.ca (X. Sun).

https://doi.org/10.1016/j.nanoen.2017.12.035
Received 8 November 2017; Received in revised form 18 December 2017; Accepted 21 December 2017
Available online 21 December 2017
2211-2855/ 

phases and how can this formation be reduced or eliminated during LFP manufacturing. In an effort to address these questions, we systematically investigate the formation and stability of $Fe_2P_2O_7$ phase on commercial powder samples by developing a procedure that includes a wide range of reaction conditions aimed at controlling or eliminating $Fe_2P_2O_7$ phase by tuning carbon coating parameters. In addition, LFP ingot sample prepared by melt casting method, with a large flat surface, is also used to obtain detailed surface chemistry changes that occur during the carbon coating process, thus providing crucial information toward important parameters that lead to changes at the surface/interface [25–28].

With fine tuning of carbon coating condition, a full diagram of $Fe_2P_2O_7$ phase existing region is outlined with respect to different coating parameters. Highly pure LFP particles with different size could be achieved by controlling the carbon coating process. From a thermodynamic point of view, we give a single unified mechanism that could be used to describe the formation of $Fe_2P_2O_7$ phase under different circumstance. Furthermore, we use LFP ingot sample to demonstrate the direct visualization of phase changes during the carbon coating process. The methodology utilized in this work on multi-element phase equilibrium systems under reducing atmosphere and/or high temperature can be useful for material systems that require control over phase purity and stability during carbon coating.

The origin of such impurity phase formation was **that** more FeLi anitisite was formed at lower temperature than high temperature solid state reactions [18-20].

## 2. Results

Detailed physical investigation of the $Fe_2P_2O_7$ phase change in different size $LiFePO_4$ (LFP) is presented in Fig. 1. LFP particles with different size were achieved by ball milling LFP ingot sample, with a range from micron (19 μm) to nano (60 nm) (Size distribution in Fig. S1). The relationship between particle size and $Fe_2P_2O_7$ formation were investigated by XRD, patterns of carbon-coated LFP powders were collected in Fig. 1**a**. Small peaks in the XRD within the range of 28–33° (grey area) increase in intensity with increasing LFP particle size. This range of peaks can be assigned to $Fe_2P_2O_7$ (JCPDS no 76-1762), suggesting that increased LFP size results in high amount of $Fe_2P_2O_7$. As LFP particle sizes decrease, $Fe_2P_2O_7$ peaks diminish and are virtually non-existent at sizes below 150 nm (See the circle inset in Fig. 1**a**). To obtain further evidence for the size-dependent relationship on the formation of $Fe_2P_2O_7$ phase, three samples of size 560 nm, 150 nm, and 60 nm were characterized using high resolution transmission electron microscope (HRTEM, Fig. 1**b**). For 560 nm LFP, two sets of diffraction patterns are observed. One can be assigned to bulk phase $LiFePO_4$ while the other is attributed to $Fe_2P_2O_7$ impurity phase (inset of 560 nm LFP in Fig. 1**b**), indicating the co-existence of these two phases. Interestingly, HRTEM reveals the presence of a thin carbon layer approximately ~2 nm in thickness. This layer is closely followed by a thin strip of $Fe_2P_2O_7$. In contrast, the smaller particles (60 nm) or the critical size (150 nm) particles show no evidence of $Fe_2P_2O_7$ impurity (150 nm LFP and 60 nm LFP in Fig. 1**b**), remaining as pure $LiFePO_4$ phase. The carbon layer covered on the two different LFP particles is ~ 5 nm (150 nm LFP) and ~ 8 nm (60 nm LFP), respectively, suggesting thicker carbon layer for a smaller LFP. It is evident that the impurity phase $Fe_2P_2O_7$ formation during carbon coating process is size dependent and the critical size is 150 nm. With such a value in mind, we can instruct the manufacturer to produce the right size for impurity free LFP with suitable tap density.

$Fe_2P_2O_7$ is an electrochemically inert phase and therefore influences electron and lithium transportation, leading to decreased capacity and cycling stability. To investigate this effect, electrochemical performance of LFP particles with different sizes were evaluated at a current density of 0.1 C (1 C = 170 mA $g^{-1}$), as shown in Fig. 1**c**. Clearly, smaller particle sizes deliver increased capacity compared to their larger-sized counter parts. For example, 19 μm LFP particles only deliver a discharge capacity of 100 mAh $g^{-1}$ in the first cycle with capacity fading to 61 mAh $g^{-1}$ after 100 cycles (capacity retention of 61%). On the contrary, the 60 nm LFP sample exhibits a very stable discharge capacity of 160 mAh $g^{-1}$, with 100% capacity retention after 100 cycles. The other different-sized LFP (from 150 nm to 560 nm) follow the same trend in between the 19 μm-size and 60 nm LFP. However, the performance here includes the influence of impurity phase and particle size. In the next section, we will exclude the influence of particle size, as the smaller size LFP is impurity free while the bigger size LFP has different level of impurity, which makes the evaluation of impurity phase difficult.

Additionally, temperature plays an important role in the formation of $Fe_2P_2O_7$ impurity phase during the carbon coating process. The 19 μm LFP particles were initially studied to determine the influence of temperature on the formation of $Fe_2P_2O_7$, Fig. 2**a** illustrated the phase change of LFP during carbon coating. XRD patterns are taken within a temperature range of 400–850 °C with a 50 °C interval. From the peaks shape between 28° and 33° in Fig. 2**a**, it can be clearly seen that the $Fe_2P_2O_7$ impurity phase changes with temperature. Diffraction peaks for $Fe_2P_2O_7$ impurities begin to appear at 450 °C and their intensities become stronger as annealing temperatures reach 750 °C. Interestingly, the diffraction peaks for $Fe_2P_2O_7$ impurity disappears at temperatures above 800 °C (inset in Fig. 2**a** in the range of 28–33°). Sensitivity of detecting $Fe_2P_2O_7$ impurity as a function of temperatures provides important insight on surface chemistry of LFP during the carbon coating process, therefore, we further investigate the phase evolutions as a function of temperature using an *in-situ* XRD heating stage (Fig. S2). From these experiments we observe the same phase change trend as *ex-situ* XRD samples, suggesting instability of $Fe_2P_2O_7$ phase at high temperature. Furthermore, we also extended the same experiment to smaller LFP particles. The similar trend of appearance and disappearance of $Fe_2P_2O_7$ impurity with temperatures is observed in LFP particles with smaller size (560 nm and 50 nm LFP) at 400–800 °C. The difference among these three size LFP samples is that the critical temperature for disappearance of $Fe_2P_2O_7$ impurity decreases with smaller LFP particle sizes. (See Fig. S3a and b).

To obtain further evidence of surface changes, sub-micron particles (560 nm LFP) were chosen as a suitable model for morphology and crystal structure investigation. From SEM images of 560 nm LFP (Fig. S3c), no obvious surface chemistry changes were observed for two different temperature (700 °C and 800 °C) coated LFP samples. Slight particle growth for samples annealed at 800 °C is observed by estimating the size-distribution, it is a phenomenon commonly found for nano LFP. Therefore, detailed structural information through HRTEM and SAED characterizations were performed to verify surface chemistry changes. A clear difference in both the SAED patterns and HRTEM images of two coated samples can be seen in Fig. 2**b**. Compared with 700 °C LFP samples, the SAED pattern for 800 °C LFP samples shows only one set of diffraction peaks, which can be identified and indexed as LFP. Furthermore, HRTEM images reveal LFP pure surface with no trace of $Fe_2P_2O_7$, covered with a thick ~ 6.6 nm carbon layer, which is consistent with XRD analysis in Fig. 2**a**.

As demonstrated earlier, LFP performance is influenced by the amount of $Fe_2P_2O_7$ impurity as well as LFP particle size. To exclude the influence of particle size, we examined the electrochemical performance of 19 μm LFP treated under different temperatures (Fig. 2**c**). It seems that electrochemical performance can be correlated to amount of $Fe_2P_2O_7$ impurity phase. Our results demonstrate that an increased amount of impurity leads to quick capacity decay and loss of reversible capacity. Furthermore, rate performance testing on the 700 °C, 800 °C samples and 750 °C sample with more $Fe_2P_2O_7$ indicates that a diminished performance is observed for 750 °C sample with the increase of impurity content, especially at higher rate. This phenomenon may be ascribed to the inert nature of $Fe_2P_2O_7$. During electrochemical cycling, $Fe_2P_2O_7$ impurity phase impedes lithium-ion mobility and inhibits its

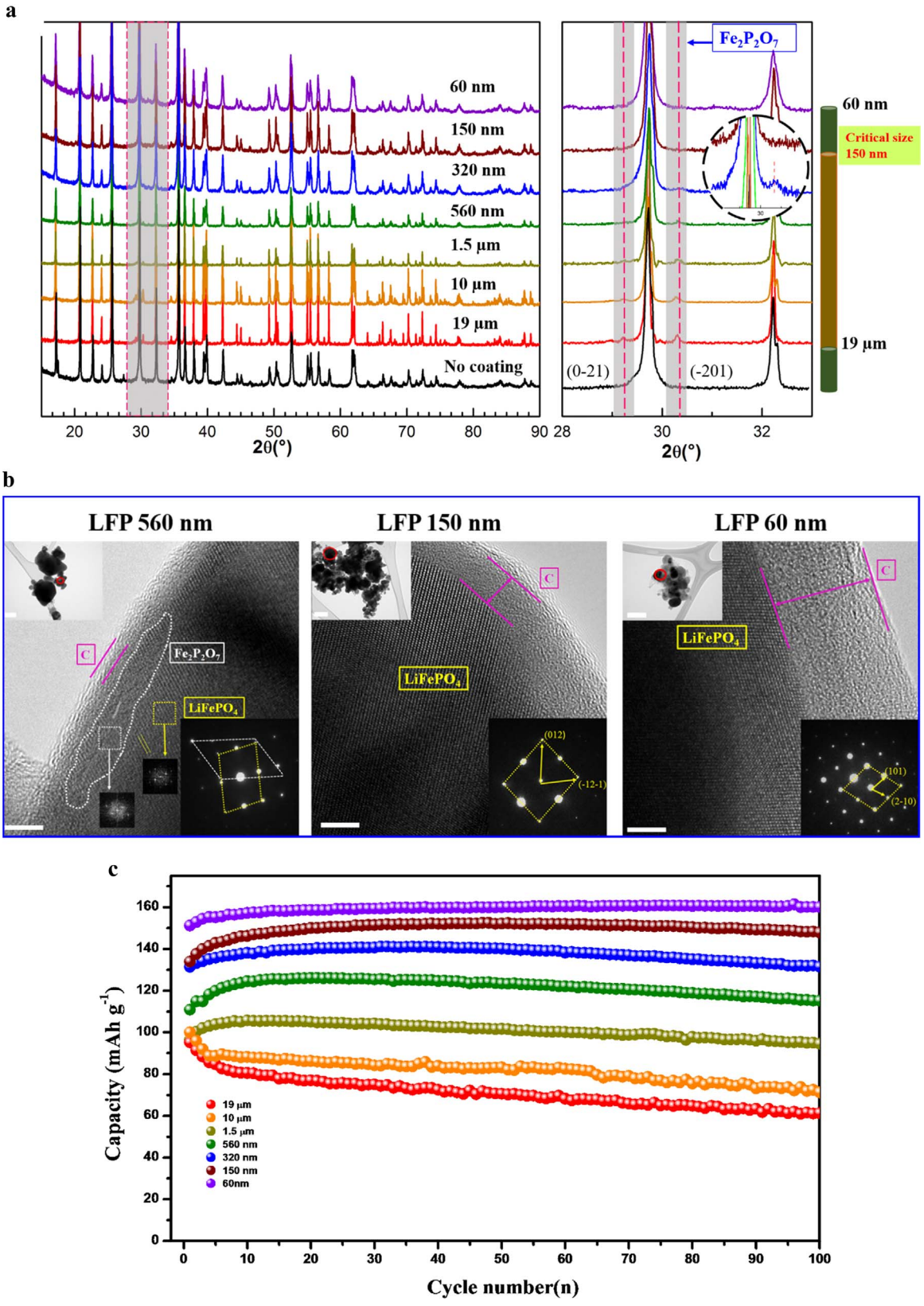


**Fig. 1.** Size dependent effect of $Fe_2P_2O_7$ impurity phase formation during carbon coating (700 °C). (a) XRD pattern of different size, from 60 nm to 19 μm. Right side shows the impurity phase region. (b)HRTEM characterization of 560 nm, 150 nm and 60 nm $LiFePO_4$ particles. Scale bar, 5 nm in HRTEM and 500, 200, 100 nm respectively in tree insert panel. (c)Cycle performance of $LiFePO_4$ particles at 0.1 C (1 C = 170 mA $g^{-1}$).

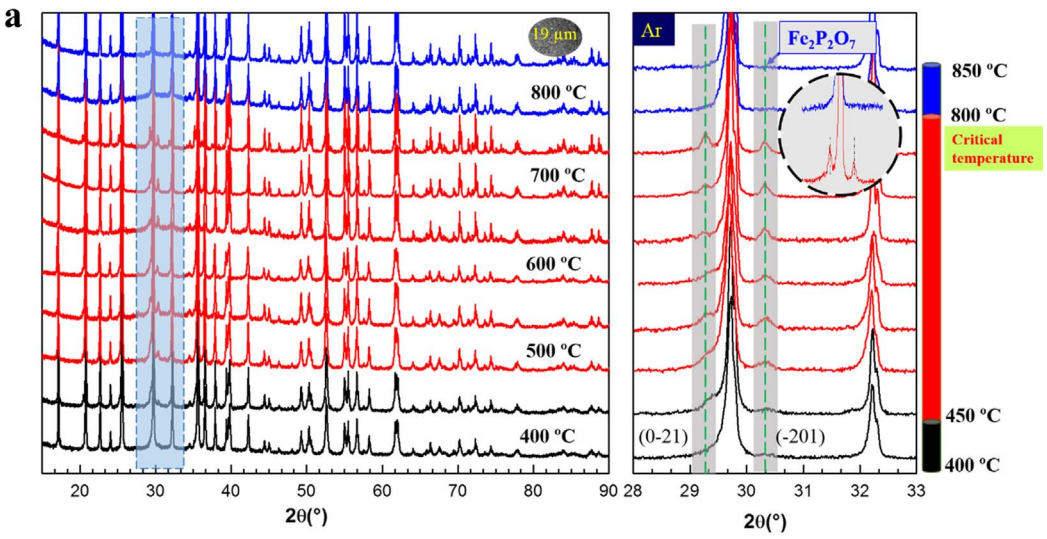


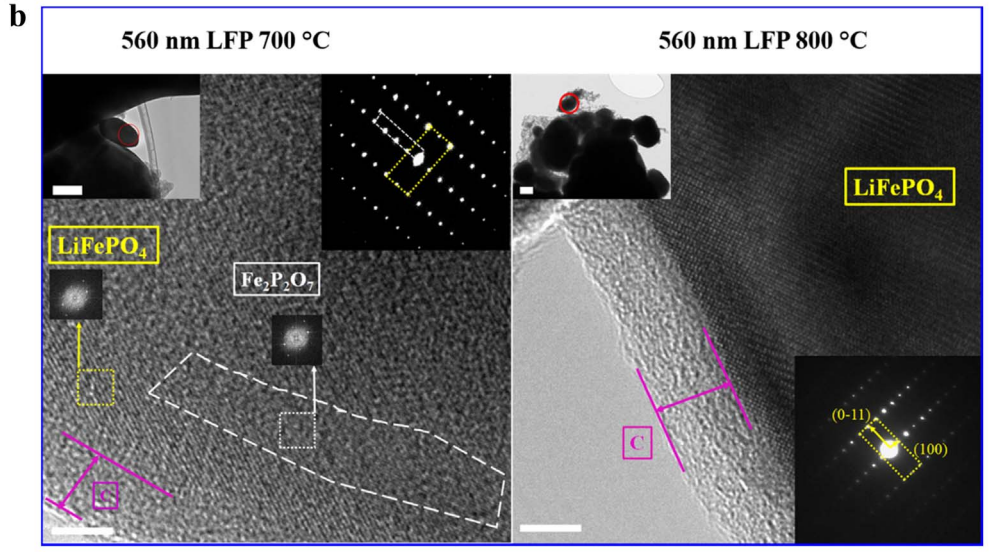


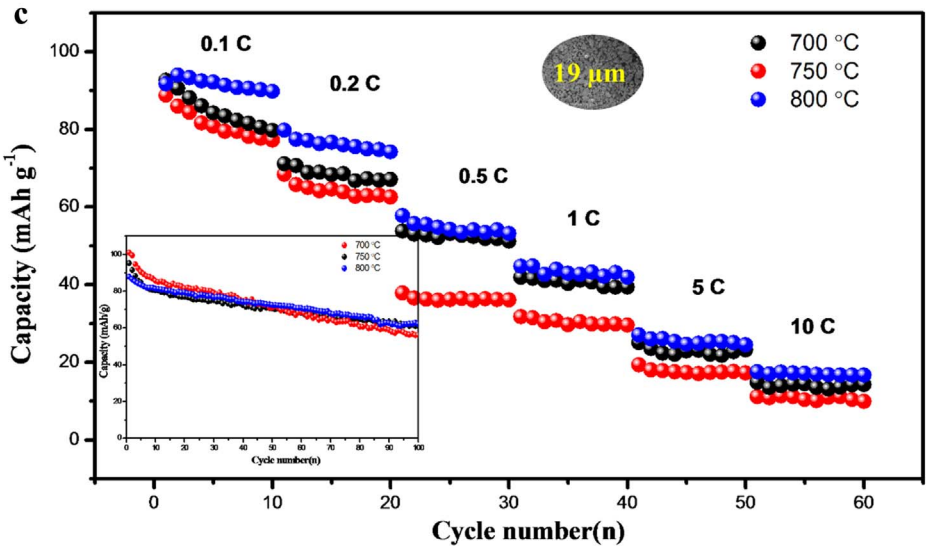


**Fig. 2.** Temperature dependent effect of $Fe_2P_2O_7$ impurity phase during carbon coating. (a)XRD pattern of micro (19 μm) LFP particles after carbon coating at different temperature. (b) HRTEM images of 560 nm C/$LiFePO_4$ particles at 700 °C and 800 °C. Scale bar, 5 nm in HRTEM, 500 nm in the insert TEM images. (c) Electrochemical performance of micro (19 μm) LFP samples annealed at three different temperatures at different rate current density (0.1 C, 0.2 C, 0.5 C, 1 C, 5 C, 10 C) (1 C = 170 mA $g^{-1}$) and long term cycle performance of 0.1 C in the inset.

ability to access active LFP. As lithiation and delithiation continues, lithium ions accumulate at the interface between the impurity layer and the active layer leading to rapid loss of capacity. However, we cannot completely rule out that the difference in electrochemical performance treated at different temperature is caused by different carbon coating quality. One possible reason for good performance for carbon coated LFP sample annealed at 800 °C is the high conductivity of the carbon layer, which can benefit for the rate capability. Further investigation is

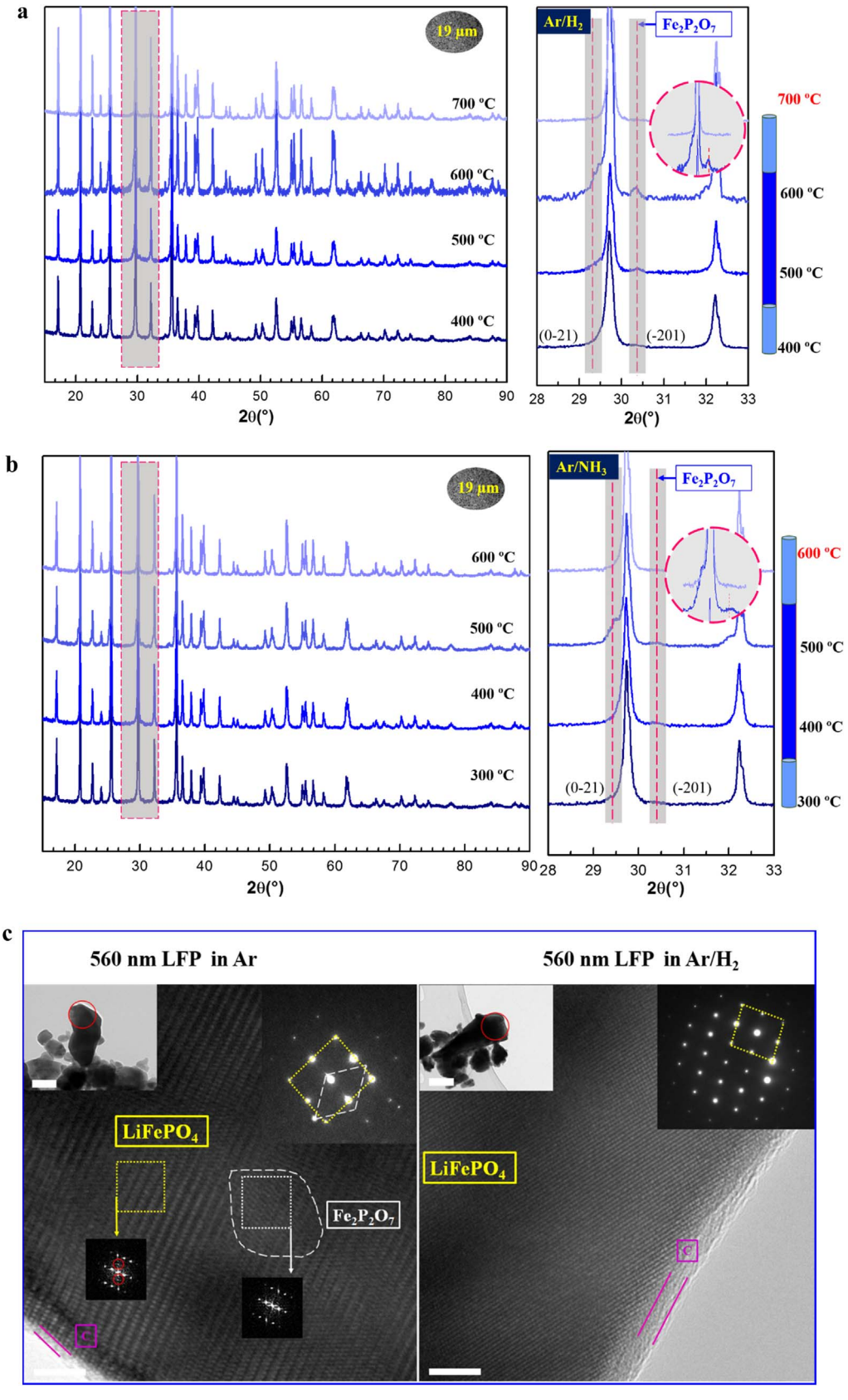


**Fig. 3.** Atmosphere dependent effect of $Fe_2P_2O_7$ impurity phase during carbon coating in 19 μm LFP. (a) $Ar/H_2$ (b) $Ar/NH_3$ (c) HRTEM images of 560 nm C/$LiFePO_4$ particles in Ar and $Ar/H_2$. Scale bar, 5 nm in HRTEM, 100 nm in the insert TEM images.

needed to confirm the blocking effect of $Fe_2P_2O_7$ phase.

Apart from effect of temperature, annealing atmosphere plays an important role in LFP carbon coating process. In an effort to reduce the amount of $Fe_2P_2O_7$ impurity phase at elevated temperature, we introduced reductive gas ($H_2$ and $NH_3$ gas) to amplify the reducing atmosphere effect on LFP. Fig. 3 illuminates the atmospheric dependent nature of $Fe_2P_2O_7$ impurity phase in LFP particles during the carbon coating process. Carbon coating were performed for 19 μm LFP in the

temperature range of 400–700 °C for $Ar/H_2$ (95:5) and 300–600 °C for $Ar/NH_3$ (95:5). XRD patterns of 19 μm LFP taken after using a $Ar/H_2$ reducing atmosphere (Fig. 3**a**) demonstrates that the critical temperature for removal of $Fe_2P_2O_7$ phase decrease from 800 °C in pure Ar to 700 °C, indicating a narrower phase stable region. For an $Ar/NH_3$ annealing atmosphere (Fig. 3**b**), critical temperature of 600 °C is observed for the removal of $Fe_2P_2O_7$ phase in 19 μm LFP. Compared to pure Ar, the appearance of $Fe_2P_2O_7$ temperature region for 19 μm LFP also decreases from a range of 500–700 °C to 400–500 °C in $Ar/NH_3$. For 560 nm LFP, $Fe_2P_2O_7$ impurity phase's region narrows down in $Ar/H_2$ and then totally diminishes in $Ar/NH_3$. (See Fig. S4, S5). More interestingly, with the reducing atmosphere of $H_2$ and $NH_3$, 60 nm LFP is completely free of $Fe_2P_2O_7$ impurity phase in the temperature range of 400–700 °C (See Fig. S4, S5).

Detailed morphology and crystal structure information of samples annealed at different atmosphere were investigated, using 560 nm-size LFP as an example. From the SEM images in Fig. S4c, no obvious surface changes and particle size changes could be observed for neither Ar nor $Ar/H_2$ atmosphere annealed 560 nm LFP samples. However, structural information from HRTEM and SAED characterizations confirm surface chemistry change following different annealing atmosphere. From SAED patterns in Fig. 3**c**, two sets of diffraction patterns of $Fe_2P_2O_7$ and LFP are presented in 560 nm LFP sample coated in Ar atmosphere whilst there is only one sets of diffraction pattern of LFP in 560 nm LFP sample coated in $Ar/H_2$ atmosphere. Furthermore, 560 nm LFP treated in an Ar atmosphere display characteristics lattice of $Fe_2P_2O_7$ impurity in the HRTEM of Fig. 3**c**, while clean surface is presented for 560 nm LFP coated in $Ar/H_2$ atmosphere.

An outline demonstrating the influence of size, temperature and atmosphere on formation of $Fe_2P_2O_7$ impurity phase during LFP carbon coating is presented in Fig. S6. From XRD patterns obtained herein, we demonstrate the ability to control the formation of $Fe_2P_2O_7$ phase and provide an avenue toward obtaining pure LFP through fine tuning important synthesis parameters. This map will instruct manufacturers as well as researchers a method toward producing impurity-free LFP.

## 3. Discussion

Fig. 4 displays the phase transition diagram for $Fe_2P_2O_7$ phase with respect to LFP particle size, annealing temperature, and annealing atmosphere. Formation temperature for $Fe_2P_2O_7$ phase, in an Ar atmosphere, remains constant from 320 nm to 19 μm until LFP particles size

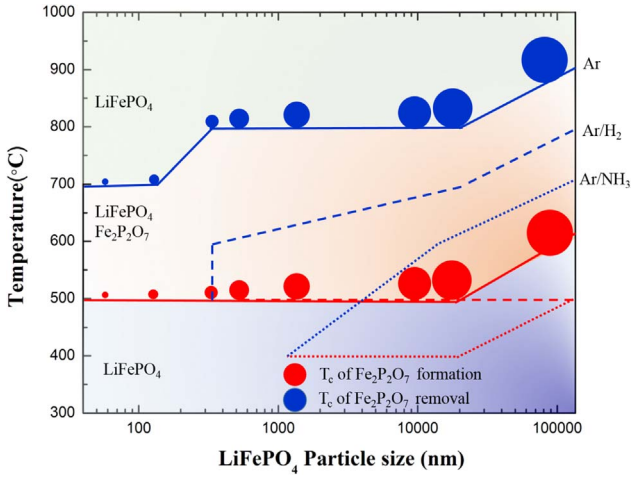


**Fig. 4.** Phase transition diagram of $Fe_2P_2O_7$ with respect to size, temperature and atmosphere. Red circles label the $Fe_2P_2O_7$ formation temperature, Tc, with change in particles size. Blue circles label the $Fe_2P_2O_7$ removal temperature, Tc, with change in particles size. Solid red and blue lines define the edge of phase transition in Ar atmosphere, dash lines define the edge of phase transition in $Ar/H_2$ and dot line define the edge of phase transition in $Ar/NH_3$.

increases into the millimeter range. On the other hand, there is an obvious difference in the temperature necessary for the removal of $Fe_2P_2O_7$ phase in smaller LFP particles. Specifically, for 150 nm and 60 nm LFP particles, the temperature necessary for removal of $Fe_2P_2O_7$ phase is suppressed down to 700 °C. More importantly, we find that the stability region of $Fe_2P_2O_7$ is further reduced with the addition of a reducing atmosphere ($H_2$ and $NH_3$). Highly pure LFP particles are easily obtained as the $Fe_2P_2O_7$ stable region in the phase diagram becomes smaller. Such a unique phase transition phenomenon should be related to interface reactions between carbon and the underlying LFP.

In our previous work, we hypothesized that smaller particles underwent a high rate of carbon deposition, resulting in rapid formation of carbon layer on the surface of LFP. This process then in-turn limited lithium depletion at surface, thereby preventing the surface change from LFP to $Fe_2P_2O_7$. On the contrary, bigger particles underwent a slow carbon deposition rate, resulting in fast lithium depletion at the surface as well as lithium evaporation during the carbon coating [24]. In light of the evidence presented herein, we offer an alternative thermodynamic interpretation for the underlying mechanism on the formation of $Fe_2P_2O_7$ phase during carbon coating (Fig. 5).

Carbon coating inherently invokes a reducing environment due to the high temperature and reducing agents involved. At relatively lower temperatures (< 300 °C), the formation of $Fe_2P_2O_7$ is unfavorable because a limited amount of hydrocarbon decomposition occurs, resulting in a small amount of reducing gas being produced. As temperature increases, the amount of reducing gas produced also increases, and formation of $Fe_2P_2O_7$ occurs more readily. More intriguing phenomenon is the stability region of $Fe_2P_2O_7$ phase under reducing environment. First principle calculation conducted by Ceder et al. [11], revealed that $Fe_2P_2O_7$ phase appears when the oxygen chemical potential reaches $\mu_{o_2} = -12.38$ eV, and disappears at $-16.08$ eV(see Supplementary information about oxygen chemical potential). Thus, $Fe_2P_2O_7$ phase has a thermodynamic stability region between oxygen chemical potential $\mu_{o_2}$ of $-12.38$ to $-16.08$. $\mu_{o_2}$ is determined by temperature and partial pressure of oxygen, simultaneously. With higher temperatures, lower oxygen partial pressures and/or the presence of reducing agent, lower value $\mu_{o_2}$ is deemed. Herein, we find that the formation of $Fe_2P_2O_7$ phase during carbon coating is dependent not only on the oxygen chemical potential, but also on the particle size of LFP samples.

In a typical carbon coating process under Ar gas, a high value of oxygen chemical potential $\mu_{o_2}$ at low coating temperature, which is unfavorable for formation of the $Fe_2P_2O_7$ phase. When $\mu_{o_2}$ approaches $-12.38$ eV at 450 °C in micro-size LFP (19 μm), the formation of $Fe_2P_2O_7$ phase begins. Therefore, the formation of $Fe_2P_2O_7$ phase becomes thermodynamically favourable as temperature increases, resulting in more crystalline $Fe_2P_2O_7$ phase in LFP. Further increasing the coating temperature (above 800 °C), $Fe_2P_2O_7$ becomes thermodynamically unstable as $\mu_{o_2}$ decreases below $-16.08$ eV. This explains the temperature-dependent phenomenon of $Fe_2P_2O_7$ phase formation during LFP carbon coating process. On the other side, $\mu_{o_2}$ is also determined by oxygen partial pressure, which could be influenced by the presence of reducing gas. For smaller sized LFP particles (560 nm and 60 nm), more reducing gas ($H_2$) is formed due to rapid decomposition of the supplied carbon, originating from high catalytic of surface Fe atoms. [24] This phenomenon is supported by the observation of a relatively thick carbon layers deposited on the surface of smaller LFP particles (HRTEM images in Fig. 1**b**). The Brunauer–Emmett–Teller (BET) surface area of LFP particle was measured through $N_2$ adsorption/desorption isotherms tests (Fig. S7 and Table S1). The results suggested that $Fe_2P_2O_7$ formation was closely related to the surface area of LFP particles.

Thus, lower $\mu_{o_2}$ value will be obtained for small-LFP particles at the same temperature of big LFP particles because presence of more reducing agent leads to lower oxygen partial pressure $P_{O_2}$. Therefore, the amount of $Fe_2P_2O_7$ formed on LFP surface decreases with particle size decreasing. Especially, 60 nm and 150 nm LFP particles are free of

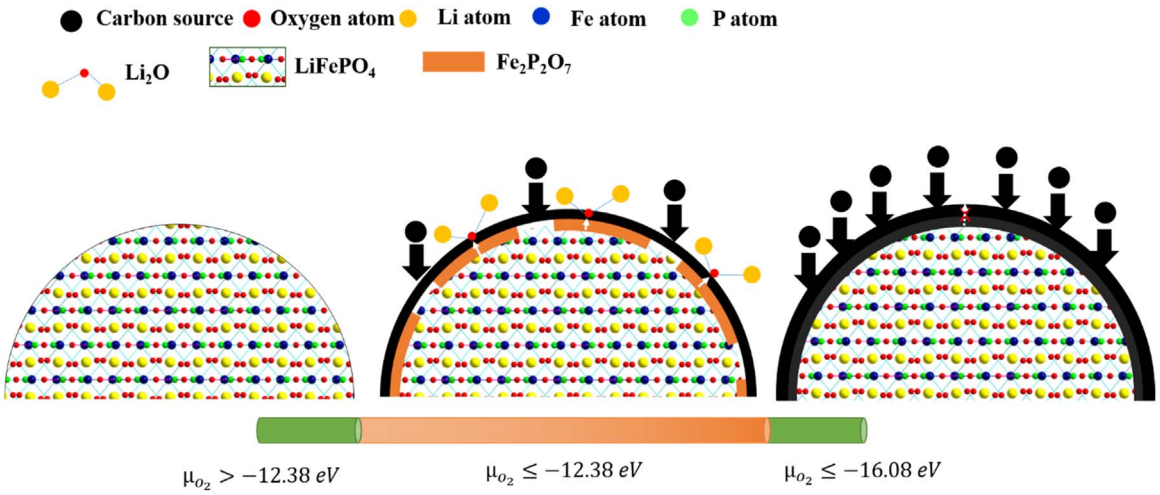


**Fig. 5.** A schematic diagram illustration of the relationship of $Fe_2P_2O_7$ transformation during carbon coating with respect to oxygen chemical potential ( $\mu_{O2}$).

$Fe_2P_2O_7$ phase because they have reached the critical $\mu_{o_2}$ value at 700 °C. When a reducing gas ($H_2$) is intentionally introduced during the LFP carbon coating process, oxygen partial pressure $P_{O_2}$ inherently decreases and the critical temperature for removal of $Fe_2P_2O_7$ for 19 μm LFP in Ar/$H_2$ declines below 700 °C. This is a result of decreasing oxygen chemical potential, which has been shown to influence the presence of $Fe_2P_2O_7$. Furthermore, $Fe_2P_2O_7$ phase is removed at even lower temperatures for smaller LFP particles (560 nm and 60 nm LFP) because *in-situ* production of more reducing $H_2$ via decomposition of the carbon source alters the oxygen partial pressure. When the reducing gas employed is ammonia ($NH_3$), both the formation and removal temperatures of $Fe_2P_2O_7$ phase are greatly reduced for all LFP particles due to a large decrease in $P_{O_2}$, resulting in decreased $\mu_{o_2}$, regardless of temperature. Therefore, atmospheric conditions during the carbon coating process is important in the formation of $Fe_2P_2O_7$ phase. Based on Cedar paper, such a $Fe_2P_2O_7$ phase change phenomenon was easily observed in Li-deficient LFP [11]. Our inductively coupled plasma atomic emission spectroscopy (ICP-AES) testing (Table S2) on LFP particles also confirms that lithium is deficient in large-sized LFP samples. Moreover, the $Fe_2P_2O_7$ phase formation is independent of carbon precursor choice as $Fe_2P_2O_7$ phase formation occurs in 19 μm -LFP with gas carbon ($C_2H_4$) as precursor (Fig. S8).

To provide further evidence for our thermodynamic mechanism, we employed LFP ingot as a model sample to study the $Fe_2P_2O_7$ phase change under different carbon coating conditions. The morphologies of LFP ingot under different carbon coating temperature are shown in Fig. S9, ranging from 600 °C to 900 °C. SEM images of samples treated at 600 °C reveal a relatively flat surface with only thin layer of carbon while samples treated at a higher temperature (700 °C) appear to have island-shaped phases distributed on the surface. The island shape phase is associated with lattice mismatch stress between surface and bulk phases. [24] Increasing the temperature to 800 °C results in the growth of these island phases. However, further increasing the temperature beyond 800 °C leads to the disappearance of island shaped phases. A detailed study on with narrower temperature step shows that the surface phase formation region begins as low as 650 °C, and end at 875 °C (Fig. S11, S12). The XRD patterns of the ingot sample also confirm phase changes occurring following the carbon coating at different temperature (Fig. S9e), where the peaks of $Fe_2P_2O_7$ phase changes in accordance with the island-phase formed on the surface of LFP ingot. In addition, Raman characterization was performed on LFP ingot after carbon coating to determine specifics information about LFP crystal structure. Raman spectra, presented in Fig. S10, reveals the presence of two different crystal structures for LFP coated at 800 °C. One is attributed to $Fe_2P_2O_7$ phase while the other is crystalline LFP. Furthermore, using Raman mapping, phase distribution of LFP and $Fe_2P_2O_7$ can be determined. The change of surface phase was also confirmed by Fe-K edge X-ray Absorption Near Edge Structure (XANES) spectra shown in Fig. S9f. The $Fe_2P_2O_7$ phase evolution process on the top of LFP ingot is illustrated in Fig. S9g. When the LFP ingot is coated at a low temperature ($\mu_{o_2}$ value bigger than − 12.38 eV), the formation of $Fe_2P_2O_7$ phase is thermodynamically unfavorable. Once the temperature increase and lower $\mu_{o_2}$ value less than − 12.38 eV is obtained, the $Fe_2P_2O_7$ phase formation begins and becomes more obvious with the decrease of $\mu_{o_2}$ value. But, if the $\mu_{o_2}$ value is lower than − 16.08 eV, the $Fe_2P_2O_7$ phase is thermodynamic unstable. Therefore, no $Fe_2P_2O_7$ phase could be observed at even higher temperature. If we extend the experimental in a reducing environment with the presence of $H_2$, as expected by the thermodynamic discussion above, the $Fe_2P_2O_7$ phase stable region is shifted to lower temperature (see Fig. S13).

In conclusion, we have shown that the formation of an impurity phase on the surface of LFP is dependent on particle size, temperature and atmosphere during the carbon coating process and is governed on the basis of thermodynamic principles. In a mild reducing atmosphere of argon gas, $Fe_2P_2O_7$ phase is formed at low temperatures and becomes unstable and disappears as temperature increases, regardless of particle size. In a more reducing atmosphere, $Fe_2P_2O_7$ is stable within a narrow temperature range for micro-size LFP particles and is easily limited for smaller-sized LFP particles. Our detailed investigation demonstrates that the phase purity of LFP can be controlled through either changing particle size, annealing temperature and/or reaction atmosphere. This investigation provides a path toward producing high-quality LFP for practical manufacturing purposes. Furthermore, such a size, temperature and atmospheric dependent surface phase change behavior may be extended to other olivine phosphate or insulated electrodes that also undergo carbon-coating.

## 4. Experimental details

### 4.1. Carbon coating on LFP

$LiFePO_4$ ingot samples were provided by Phostech Lithium Inc. (Now, Johnson Matthey, Montreal, Canada). The carbon coating procedure used can be found in our previous report [24].

LFP ingot was used as a base material that was cut into smaller sizes. Ingot samples were used for two reasons: the first is its commercial availability, and the second is that an ingot offers a flat, smooth and polished surface that is ideal for observing and investigating surface phase changes following carbon coating. Experimental details regarding the melt-casting process employed for obtaining LFP ingot can be found in previous work [27,28]. In order to obtain a flat surface, ingot

samples were polished using coarse (Grit 120) to fine grade (Grit 1500) sandpaper (London, 3M Canada). The polished samples were then cleaned in an ultra-sonicator using an ethanol solution.

LFP ingots were then ball-milled in isopropyl alcohol for various times using $ZrO_2$ balls to obtain LFP powder with different sizes. Following ball-milling, the obtained samples were dried in a vacuum oven prior to carbon coating.

Carbon-coating of ingot samples was performed using a spray-pyrolysis system, which was previously developed for the synthesis of various nanomaterials. Alcohol was used as a carbon precursor with Ar as a carrier gas. Briefly, ingot samples were placed in an $Al_2O_3$ crucible and loaded into a quartz tube. The ends of the tube were capped using vacuums gear and Ar (with $H_2$, $NH_3$) was introduced for 20 min to eliminate the air. Next, the furnace was heated at a heating rate of 5 °C/min, and the carbon-coating process was performed at temperatures ranging from 300 °C to 900 °C for 20 min. After the carbon coating process, the coated samples were cooled to room temperature in the same Ar atmosphere and then removed from the quartz tube.

Carbon coating of LFP powders was performed in a similar manner to ingot samples but lactose was employed as a carbon source rather than alcohol. LFP powders were homogenously mixed with lactose using water or isopropyl alcohol. The suspension was then mixed ultrasonically, and was then allowed to evaporate to dryness. The samples were annealed in Ar (with $H_2$, $NH_3$) atmosphere at a ramp rate of 5 °C/min at 300 °C to 900 °C for 1 h.

### 4.2. Physical characterization

Crystal structure and phase composition of carbon coated LFP were collected using X-ray diffraction (D8 Advance, Bruker) in the range of 10–90° with a step of 0.01° per seconds. Slow scans in the range of 28–33° were also performed to provide detail on the formation of impurity phases. The carbon coated LFP powders were also investigated using Hitachi 4800 SEM equipped with an energy dispersive spectroscopy (EDS) detector. The working voltage employed for EDS mapping was 20 kV. Raman spectra was obtained using a HORIBA Scientific LabRAM equipped with a 532.3 nm laser excitation source. Raman spectroscopy maps were collected in autofocus mode with a spatial resolution of ca. 2 μm. The detailed structure of carbon coated LFP particles were investigated using HRTEM (JEOL 2010 FEG) operating at an accelerating voltage of 20 kV while diffraction patterns were recorded using SAED mode. The X-ray absorption spectroscopy (XAS) measurements were carried out at the Canadian Light Source (CLS) using the Soft X-ray Microcharacterization Beamline (SXRMB) at the University of Saskatoon, Saskatoon, Canada. Measurements were carried out under vacuum conditions ($10^{-7}$ Torr) in either total fluorescence yield (FLY, bulk sensitive) mode and total electron yield (TEY, surface sensitive – 5 nm) mode. $N_2$ adsorption/desorption isotherms of LFP particles were performed using a Folio Micromeritics TriStar II Surface Area and Pore Size Analyzer.

### 4.3. Electrochemical tests

The electrochemical performance of carbon coated LFP were tested in 2032 coin cells, using a Li metal foil as a counter electrode. The electrode is composed of 80 wt% carbon coated LFP as active material, 10 wt% PvDF as binder, and 10 wt% carbon black as conductive agent, with an active material loading of 1.5–2 mg $cm^{-2}$. 1 M $LiPF_6$ in EC, DEC, and EMC with a volume ratio of 1:1:1 was employed as an electrolyte along with Celgard 2400 as a separator. Cells were assembled in an Ar-filled glove box with oxygen and water levels below 1 ppm. Charge-discharge cycling using a constant current mode was performed on an Arbin BT-2000 Battery Test System. All the electrochemical measurements were carried out in a voltage range of 2.2–4.2 V at RT.

## Acknowledgements

This work was supported by the Natural Sciences and Engineering Research Council of Canada (NSERC), Johnson Matthey (Previous Phostech Lithium Inc.), Canada Research Chair (CRC) Program, Canadian Light Source (CLS), McMaster Microscopy Centre for HRTEM and Western University.

## Appendix A. Supporting information

Supplementary data associated with this article can be found in the online version at http://dx.doi.org/10.1016/j.nanoen.2017.12.035.

## References

[1] N. Ravet, A. Abouimrane, M. Armand, Nat. Mater. 2 (2003) (702-702).
[2] S.-Y. Chung, J.T. Bloking, Y.-M. Chiang, Nat. Mater. 1 (2002) 123–128.
[3] Z. Chen, J. Dahn, J. Electrochem. Soc. 149 (2002) A1184–A1189.
[4] N. Ravet, Y. Chouinard, J. Magnan, S. Besner, M. Gauthier, M. Armand, J. Power Sources 97 (2001) 503–507.
[5] J. Wang, X. Sun, Energy Environ. Sci. 5 (2012) 5163–5185.
[6] J. Wang, X. Sun, Energy Environ. Sci. 8 (2015) 1110–1138.
[7] M. Herstedt, M. Stjerndahl, A. Nytén, T. Gustafsson, H. Rensmo, H. Siegbahn, N. Ravet, M. Armand, J.O. Thomas, K. Edström, Electrochem. Solid-State Lett. 6 (2003) A202–A206.
[8] R. Dominko, M. Bele, M. Gaberscek, M. Remskar, D. Hanzel, S. Pejovnik, J. Jamnik, J. Electrochem. Soc. 152 (2005) A607.
[9] B. Kang, G. Ceder, Nature 458 (2009) 190–193.
[10] P. Axmann, C. Stinner, M. Wohlfahrt-Mehrens, A. Mauger, F. Gendron, C.M. Julien, Chem. Mater. 21 (2009) 1636–1644.
[11] S.P. Ong, L. Wang, B. Kang, G. Ceder, Chem. Mater. 20 (2008) 1798–1807.
[12] C.M. Julien, A. Mauger, K. Zaghib, J. Mater. Chem. 21 (2011) 9955–9968.
[13] P.S. Herle, B. Ellis, N. Coombs, L.F. Nazar, Nat. Mater. 3 (2004) 147–152.
[14] S.-Y. Chung, J.T. Bloking, Y.-M. Chiang, Nat. Mater. 1 (2002) 123–128.
[15] K. Zaghib, A. Mauger, F. Gendron, C.M. Julien, Chem. Mater. 20 (2008) 462–469.
[16] M.M. Doeff, Y. Hu, F. McLarnon, R. Kostecki, Electrochem. Solid-State Lett. 6 (2003) A207.
[17] N. Ravet, M. Gauthier, K. Zaghib, J.B. Goodenough, A. Mauger, F. Gendron, C.M. Julien, Chem. Mater. 19 (2007) 2595–2602.
[18] A. Paolella, S. Turner, G. Bertoni, P. Hovington, R. Flacau, C. Boyer, Z. Feng, M. Colombo, S. Marras, M. Prato, L. Manna, A. Guerfi, G.P. Demopoulos, M. Armand, K. Zaghib, Nano Lett. 16 (2016) 2692–2697.
[19] A. Paolella, G. Bertoni, P. Hovington, Z. Feng, R. Flacau, M. Prato, M. Colombo, S. Marras, L. Manna, S. Turner, G. Van Tendeloo, A. Guerfi, G.P. Demopoulos, K. Zaghib, Nano Energy 16 (2015) 256–267.
[20] S.-Y. Chung, S.-Y. Choi, T.-H. Kim, S. Lee, ACS Nano 9 (2015) 850–859.
[21] A.A. Salah, A. Mauger, C.M. Julien, F. Gendron, Mater. Sci. Eng.: B 129 (2006) 232–244.
[22] L.-X. Yuan, Z.-H. Wang, W.-X. Zhang, X.-L. Hu, J.-T. Chen, Y.-H. Huang, J.B. Goodenough, Energy Environ. Sci. 4 (2011) 269–284.
[23] Y. Wang, P. He, H. Zhou, Energy Environ. Sci. 4 (2011) 805–817.
[24] J. Wang, J. Yang, Y. Tang, J. Liu, Y. Zhang, G. Liang, M. Gauthier, Y.-cK. Chen-Wiegart, M.N. Banis, X. Li, Nat. Commun. 5 (2014) 3415–3423.
[25] J. Wang, J. Yang, Y. Tang, R. Li, G. Liang, T.-K. Sham, X. Sun, J. Mater. Chem. A 1 (2013) 1579–1586.
[26] J. Wang, J. Yang, Y. Zhang, Y. Li, Y. Tang, M.N. Banis, X. Li, G. Liang, R. Li, X. Sun, Adv. Funct. Mater. 23 (2013) 806–814.
[27] M. Gauthier, C. Michot, N. Ravet, M. Duchesneau, J. Dufour, G. Liang, J. Wontcheu, L. Gauthier, D. MacNeil, J. Electrochem. Soc. 157 (2010) A453–A462.
[28] D. MacNeil, L. Devigne, C. Michot, I. Rodrigues, G. Liang, M. Gauthier, J. Electrochem. Soc. 157 (2010) A463–A468.

**Yulong Liu** is currently postdoctoral fellow in Prof. Xueliang (Andy) Sun' Nanomaterials and Energy Group at the University of Western Ontario, Canada. He received his Bachelor degree from Central South University, China, in 2010, and Master degree in 2013. In 2017, he obtained his Ph.D. degree in Materials Science and Engineering from University of Western Ontario. His research interests include nanomaterials for lithium ion batteries, especially $LiFePO_4$ (in collaboration with Phostech Lithium previously and now with *Johnson Matthey)*, and the development of the solid state batteries.

**Jiajun Wang** is currently a professor at Harbin Institute of Technology (HIT), China. Prior to joining to HIT, he was a synchrotron beamline scientist at National Synchrotron Light Source, Brookhaven National Laboratory and then Advanced Photon Source, Argonne National Laboratory to develop *in situ/in operando* synchrotron X-ray imaging techniques for energy material research. He has published over 80 papers with over 4000 citations. His research activities include synchrotron X-ray technologies, phase transition, electrochemistry, engineering materials, nanoparticles and nanocomposites, energy storage and conversion materials.

**Jian Liu** is an Assistant Professor at the University of British Columbia (UBC) Okanagan campus, Canada. Dr. Liu received his Ph.D. in materials science in 2013 from the University of Western Ontario (Canada), and worked as a NSERC Postdoctoral Fellow at Lawrence Berkeley National Laboratory and Pacific Northwest National Laboratory (USA) prior to joining UBC in January 2017. His current research interests focus on advanced nanofabrication techniques, materials design for Li-ion batteries.

**Mohammad Norouzi Banis** is research engineer in Prof. Xueliang (Andy) Sun's group at University of Western Ontario, Canada. He received his Ph.D. degree in 2013 in Materials Science and Engineering from Western University, on the study of nanostructured low temperature fuel cells and application of x-ray absorption spectroscopy in energy related systems. His current research interests include study of metal ion, metal air and nanocatalysts via in-situ synchrotron based techniques.

**Biwei Xiao** is currently a postdoctoral research associate at the Pacific Northwest National Laboratory. He received his Ph.D. in 2017 from University of Western Ontario in Canada. His research interests are associated with the synthesis, modification and mechanism study of electrode materials for sodium-ion batteries and lithium-ion batteries, atomic layer deposition, synchrotron radiation technique and carbonaceous materials.

**Andrew Lushington** is currently a Ph.D. candidate in prof. Xueliang (Any) Sun's Nanomaterials and Energy Group at the University of Western Ontario. He received his BSc in Chemistry with a Concentration in Nanotechnology and a minor in Religion from Carleton University (Ottawa, Canada) in 2012. His current research interest is predominantly in the area of atomic and molecular layer deposition for the application and use in energy storage and energy conversion devices.

**Wei Xiao** received his bachelor degree of Metallurgical Engineering in 2010 and master degree of Electrochemical Engineering in 2013 at Central South University, China. He then joined Prof. Xueliang (Andy) Sun's group to pursue a PhD in Department of Mechanical and Materials Engineering at the University of Western Ontario. His main research interests involve the development of high-performance anode materials for lithium/sodium-ion batteries. He is co-supervised by Prof. Tsun-Kong Sham in Department of Chemistry. His current research works are also related to advanced characterizations on electrochemical systems and energy materials via synchrotron-based X-ray techniques.

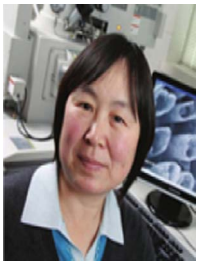

**Ruying Li** is a research engineer at Prof. Xueliang (Andy) Sun's Nanomaterial and Energy Group at the University of Western Ontario, Canada. She received her master in Material Chemistry under the direction of Prof. George Thompson in 1999 at University of Manchester, UK, followed by work as a research assistant under the direction of Prof. Keith Mitchell at the University of British Columbia and under the direction of Prof. Jean-Pol Dodelet at l'Institut national de la recherché scientifique (INRS), Canada. Her current research interests are associated with synthesis and characterization of nanomaterials for electrochemical energy storage and conversion.

**Tsun-Kong Sham**, OC, PhD, FRSC, is Distinguished University Professor and Canada Research Chair at Western University with a PhD from the University of Western Ontario and a B.Sc. in Chemistry from the Chinese University of Hong Kong. He returned to Western University in 1988 after a span of a decade at Brookhaven National Laboratory. His research interests are materials and synchrotron radiation. Expertise include nanomaterials, bimetallic systems, surface and interface, photoemission, X-ray absorption, photon-in photon-out and X-ray microscopy. Recent interests include nanostructure phase transition, in situ/ in operando studies of energy materials and devices, nanomaterials for drug delivery, and microbeam analysis of cultural and heritage materials.

**Guoxian Liang** received his Ph.D. in materials science and metallurgy from Harbin Institute of Technology in 1992, followed by working as an associate professor there until end of 1995. After that he was involved in hydrogen storage for 10 years at Laval University, Hydro-Quebec and HERA hydrogen storage systems Inc. In 2006, he joined Phostech lithium as R&D manager to support the growth of $LiFePO_4$ business, and now he acts as technology manager for the $LiFePO_4$ commercial plant in Canada, owned by Johnson Matthey.

**Xueliang (Andy) Sun** is a Canada Research Chair in Development of Nanomaterials for Clean Energy, Fellow of the Royal Society of Canada and Canadian Academy of Engineering and Full Professor at the University of Western Ontario, Canada. Dr. Sun received his Ph.D. in materials chemistry in 1999 from the University of Manchester, UK, which he followed up by working as a postdoctoral fellow at the University of British Columbia, Canada and as a Research Associate at L'Institut National de la Recherche Scientifique (INRS), Canada. His current research interests are focused on advanced materials for electrochemical energy storage and conversion, including electrocatalysis in fuel cells and electrodes in lithium-ion batteries and metal–air batteries.